

# Polydisperse collision kernels in droplet-laden turbulence with implications for rain formation

Lukas A. Codispoti,\* Daniel W. Meyer, and Patrick Jenny

*Institute of Fluid Dynamics, ETH Zürich  
Sonneggstrasse 3, 8092 Zürich, Switzerland*

(Dated: March 16, 2026)

The collision kernel of droplets in warm clouds is a crucially important quantity for the parameterization of precipitation in weather and climate models. Nevertheless, its accurate representation remains a challenge, specifically in the bottleneck range  $15\ \mu\text{m} < r < 40\ \mu\text{m}$ , within which turbulence is believed to substantially contribute to droplet growth. In this work, we address this problem by performing direct numerical simulations of polydisperse inertial particles suspended in three-dimensional turbulence at Reynolds number up to  $Re_\lambda = 418$ . Collision statistics are compiled for droplet pairs across the Stokes number range  $St \in [0.02, 2]$ , yielding comprehensive bidisperse maps of collision kernels, radial relative velocities, and radial distribution functions at contact. Our analysis reveals that polydispersity enhances collisions between light droplets through differential sampling, but attenuates collisions at larger Stokes numbers by rapidly reducing the spatial overlap of droplet clusters. By benchmarking existing models, we show that dominant bidisperse errors arise from overpredicted cross-species clustering. In light of these results, we propose an adapted model for the bidisperse radial distribution function, as well as a novel parameterization for the associated collision kernel, applicable to the smallest droplets in the bottleneck range with small settling velocities. Finally, we study the broadening of the droplet size distribution due to collision-coalescence and demonstrate that droplet growth is markedly accelerated in parcels of large local dissipation rate, supporting the hypothesis that turbulent intermittency may help overcome the bottleneck barrier.

## I. INTRODUCTION

Cumulus clouds form in the shallow regions of Earth's atmosphere when moist air ascends and cools, causing water vapor to condense at nucleation sites into micron-sized droplets that subsequently grow and, eventually, fall to the ground as rain. Despite this seemingly simple picture, key aspects of cloud-droplet growth remain poorly understood, contributing to persistent uncertainty in weather and climate predictions [1]. One long-standing question is how droplets with radii  $15\ \mu\text{m} < r < 40\ \mu\text{m}$  in warm (ice-free) clouds can grow rapidly enough to initiate precipitation within roughly 30 minutes, since neither condensational growth nor collision-coalescence driven by gravitational settling is sufficiently effective in this so-called *bottleneck* range [2]. Increasing evidence suggests that turbulence, the chaotic motion of fluid flow, plays an important role in resolving this puzzle. The broad range of turbulent flow scales alters the spatial distribution of droplets and amplifies relative velocities, thus increasing collision-coalescence rates compared to quiescent conditions. These enhanced rates are quantified by collision kernels, which describe how frequently droplets of given sizes encounter and collide. Accurate models for the collision kernel are essential for cloud microphysics schemes in weather and climate simulations, as they directly govern the evolution of the droplet size distribution (DSD). Developing reliable parameterizations nevertheless remains challenging due to the limited theoretical understanding of droplet-turbulence interactions, scarce in situ observations, and numerical constraints.

Warm clouds are dilute suspensions of small droplets, whose motion can be approximated by that of inertial particles in turbulence. Their finite response time

$$\tau_p = \frac{2r^2 \rho_p}{9\nu \rho_f}, \quad (1)$$

leads to dynamics that differ from those of passive fluid tracers. Here,  $\nu$  is the kinematic viscosity of the flow, and  $\rho_p$  and  $\rho_f$  denote the density of the particle and the flow, respectively. There exists a large body of literature on the motion of inertial particles in turbulence (e.g., Refs. [3–6]). In the context of droplet collisions, turbulence acts primarily through three closely related mechanisms: preferential concentration, which alters the spatial distribution of droplets; polydispersity, which enhances relative motion between droplets with different  $\tau_p$  through differential

---

\* lukasco@ethz.ch

sampling of the flow; and the sling effect, whereby droplet trajectories cross at large relative velocities in rare extreme events.

Preferential concentration arises due to the interaction of inertial particles with turbulent vortices, leading to non-uniform spatial distributions, also referred to as *clustering*. Particles tend to be expelled from regions of large vorticity and accumulate in strain-dominated areas, creating a compressible effective flow of particles [3]. The inertia of a particle is quantified by the Stokes number  $St = \tau_p/\tau_\eta$ , where  $\tau_\eta = \sqrt{\nu/\varepsilon}$  is the Kolmogorov time, characterizing the timescale of the dissipative scales, and  $\varepsilon$  is the turbulent kinetic energy dissipation rate. A particle with  $St \ll 1$  behaves like a fluid tracer, whereas with  $St \gg 1$ , particles move ballistically and decorrelate from the carrier flow. In both limits, particles disperse uniformly in space. In between the two extremes and most notably around  $St \approx 1$ , on the other hand, particles cluster (e.g., Refs. [4–6]), which naturally increases collision rates between inertial by increasing the likelihood of encounters in regions of high number density.

Polydispersity, the presence of particles with varying sizes, introduces an additional mechanism affecting collisions. Because particles of different sizes interact differently with turbulent structures, their trajectories decorrelate, leading to increased relative velocities. At the same time, differently sized particles tend to cluster in different regions of the domain, thereby reducing inter-species preferential concentration. From a phenomenological standpoint, polydispersity merits investigation since cloud droplets are inherently size-distributed in nature. While this mechanism has been studied numerically in two-dimensional turbulence (e.g., Ref. [8]) and three-dimensional turbulence at low Reynolds numbers (e.g., Refs. [9, 10]), comprehensive three-dimensional analyses at high Reynolds numbers remain limited due to computational constraints. In the present work, we extend these efforts by conducting a detailed investigation of polydisperse collision dynamics in three-dimensional turbulence at high Reynolds number.

Finally, the sling effect [11] is the mechanism through which particles experience rare extreme turbulent events and are “slung” out of vortices. This phenomenon occurs when particles from different flow regions cross trajectories, creating singularities in phase space, so-called *caustics* [12]. Caustic formation naturally leads to collisions between particles that travel on different branches of the phase-space manifold, i.e., exhibit different velocities while occupying the same location in physical space. The occurrence of caustics implies that inertial particles do not move on a continuum; thus, there is no well-defined Eulerian field that can describe the motion of the particles. Caustics in turbulent suspensions have been confirmed both numerically [13, 14] and experimentally [15]. Yet, whether the sling effect is effective for the collision-coalescence of cloud droplets has been the subject of debate in recent years [16–18].

A central question is how the effects of turbulence and gravitational settling compete in inducing droplet collisions. Their relative importance is given by the settling parameter  $Sv = \tau_p g / u_\eta$ , where  $g$  is the gravitational acceleration and  $u_\eta = (\varepsilon\nu)^{1/4}$  is the Kolmogorov velocity. Under typical conditions in cumulus clouds, the mean dissipation rate is moderate,  $\langle \varepsilon \rangle \leq 0.05 \text{ m}^2/\text{s}^3$  [19]. For droplets with radii  $r \gtrsim 15 \mu\text{m}$ , this corresponds to  $Sv > 1$ , so that gravitational settling is more important relative to turbulence. Importantly, however, this does not imply rapid collisional growth: in the bottleneck range, both turbulence-induced inertial effects and gravitational settling remain weak in absolute terms.

This picture changes when one moves away from mean conditions and considers the strong spatial variability in clouds. Measurements in atmospheric clouds are becoming available at ever-increasing resolutions, revealing evidence that a fraction of droplets experiences local conditions conducive to inertial clustering and caustic formation, even when average conditions would suggest otherwise [19, 20]. One natural source of such conditions is intermittency in the local energy dissipation rate. Since  $St \propto r^2\varepsilon^{1/2}$  and  $Sv \propto r^2\varepsilon^{-1/4}$ , inertial effects increase with  $\varepsilon$ , while reducing the relative importance of settling. Physically, the settling velocity of a droplet is unchanged, whereas the characteristic turbulent velocity increases; as a result, turbulence can become dynamically important in sufficiently intense local turbulence even for droplets that, under mean conditions, would appear to be governed primarily by gravity. Observations support the prevalence of such heterogeneous conditions. For example, Thiede et al. [20] report pronounced inertial clustering within parcels on the order of centimeters, while Allwayin et al. [21] reveal that local DSDs can be unexpectedly narrow, deviating significantly from integral-scale averages. Accelerated growth of a small subset of fortuitous droplets experiencing rare intense turbulence may also connect to the *lucky droplet hypothesis* [22], according to which warm-rain initiation is controlled not by mean statistics but by the fat tails of the relevant probability distributions. Understanding collision dynamics in this intermittent regime is therefore highly relevant to the bottleneck problem.

In this study, we perform an extensive DNS campaign of fully-resolved, three-dimensional particle-laden turbulence at  $Re_\lambda = 55, 179$  and  $418$ . Our aim is to elucidate the turbulent mechanisms governing droplet collisions in the bottleneck regime of warm-cloud microphysics. In particular, we provide what is, to our knowledge, the most extensive map of the bidisperse collision kernel obtained from high-Reynolds-number DNS to date, covering droplet pairs within the range  $St \in [0.02, 2]$ . We compare our results to existing models and propose modifications for the expression of bidisperse clustering as well as a novel parameterization for the bidisperse collision kernel. To isolate the turbulent enhancement of droplet collisions, gravity is neglected throughout much of this work. In Sec. IV B 3, however, it is reintroduced, and we show that the proposed parameterization remains qualitatively predictive for settling droplets

within the bottleneck range. Finally, we examine the evolution of the DSD and the impact of locally enhanced dissipation in simulations of coalescing, settling droplets.

Before we begin, a few remarks are warranted regarding the influence of the Reynolds number and turbulent intermittency. Atmospheric clouds exhibit Taylor-scale Reynolds numbers of  $\mathcal{O}(Re_\lambda) = 10^4$ , which are unattainable in DNSs with today's computing capabilities (fully resolving turbulence at  $Re_\lambda = 10^4$  would require  $\mathcal{O}(10^2)$  PB of memory). A systematic variational analysis of the impact of the Reynolds number is beyond the scope of this work. Prior work shows  $Re_\lambda$ -insensitivity of clustering for  $St \leq 0.2$ , modest attenuation for  $0.4 \leq St \leq 1$ , and enhancement for  $St \geq 2$  as turbulent intermittency increases with the Reynolds number [23–25]. Similar trends appear in the collision statistics [26]. The results suggest that  $Re_\lambda$  mainly affects cloud microphysics by reshaping the distribution of the local dissipation (its intermittency), not by altering the small-scale mechanics at fixed  $St$ . In other words, the dominant influence of the Reynolds number is statistical through the intermittency of  $\varepsilon$  rather than dynamical at the droplet-scale. In this work, we compute the collision statistics within simulation domains that correspond to physical cloud parcels on the scale of decimeters. At fixed volume-averaged dissipation rate, the collision dynamics within these control volumes are largely insensitive to  $Re_\lambda$ .

## II. TURBULENT COLLISION KERNEL

We consider collisions between droplet pairs  $(i, j)$  with radii  $(r_i, r_j)$ , separated by the distance  $\Delta \mathbf{x} = \mathbf{x}_i - \mathbf{x}_j$  with the relative velocity  $\Delta \mathbf{v} = \mathbf{v}_i - \mathbf{v}_j$ . The number of collisions per unit time is given by the collision rate  $\mathbb{N}_{ij}$ , and the dynamic collision kernel

$$\Gamma_{ij} = \frac{\mathbb{N}_{ij}}{n_i n_j} \quad (2)$$

is thence obtained by normalizing with the respective number densities,  $n_i$  and  $n_j$ , with an additional factor of 2 in the monodisperse case ( $i = j$ ). The widely used kinematic formulation [27, 28]

$$\Gamma = 2\pi R^2 \langle w_r \rangle g(R) \quad (3)$$

serves as the basis for most modeling approaches. Here,

$$w_r = \left. \frac{|\Delta \mathbf{v} \cdot \Delta \mathbf{x}|}{|\Delta \mathbf{x}|} \right|_{|\Delta \mathbf{x}|=R} \quad (4)$$

is the radial relative velocity (RRV) and  $g(R)$  is the radial distribution function (RDF) at contact distance  $R = r_i + r_j$ . The RDF quantifies the degree of preferential concentration. Its bidisperse form is symmetric ( $g_{ij}(r) = g_{ji}(r)$ ) and is computed as

$$g_{ij}(r) = \frac{\langle N_j \rangle_i(r) / V_s}{N_{ij} V}, \quad (5)$$

where  $\langle N_j \rangle_i(r)$  is the mean number of particles of species  $j$  at separation  $r$  from a particle of species  $i$  within the spherical shell of volume  $V_s = \frac{4\pi}{3}[(r + s/2)^3 - (r - s/2)^3]$  and thickness  $s$ ,  $N_{ij}$  is the total number of  $(i, j)$  pairs, and  $V$  is the total system volume. Essentially, Eq. (3) states that the combined effects of differential sampling, preferential concentration and the sling effect can be represented by the product  $\langle w_r \rangle g(R)$ . A common association is that differential sampling and the sling effect primarily affect the relative velocity statistics and therefore mainly enter through  $\langle w_r \rangle$ , whereas preferential concentration manifests itself in the RDF. However, this separation is not strictly valid: caustics also contribute to clustering [29], and polydispersity simultaneously increases relative velocities while modulating preferential concentration, as we will show in the present work.

Due to the massive separations of length scales of atmospheric flows, precipitation must be parameterized in weather and climate models rather than resolved directly. Large-eddy simulations (LESs) with grid spacing of  $\mathcal{O}(10)$  m have become the tool of choice to numerically investigate cloud droplet growth and to develop parameterizations for coarser-resolution simulations. Within LES frameworks, the collision kernel is central, because it directly controls the conversion of small droplets into larger ones. Typically, the kinematic form (Eq. (3)) is adopted, with  $\langle w_r \rangle$  and  $g(R)$  modeled separately based on droplet properties and local flow conditions. For example, two recent studies [30, 31] have applied this approach showed that turbulence markedly broadens the droplet size distribution in convective clouds. Both relied on the celebrated kernel of Ayala et al. [32]. However, the Ayala kernel was developed for droplets with settling parameters  $St > 1$ , where gravitational effects dominate over turbulent interactions. Further developments are therefore needed to represent turbulence-enhanced collisions across the full range of droplet sizes relevant for warm-rain formation, and to account for the influence of turbulent intermittency.

### A. Onishi framework for the turbulent collision kernel

We proceed with a discussion of the Onishi framework for the turbulent collision kernel, which serves as the main reference model in the comparisons that follow. Originally proposed by Onishi et al. [24] and later refined by Onishi & Seifert [25], it represents, to the best of our knowledge, the most comprehensive and advanced model of the turbulent collision kernel currently available for non-settling droplets. The framework combines three separate models: an original formulation for the monodisperse RDF, an expression for the bidisperse RDF following Zhou et al. [10], and the model for the RRV following Wang et al. [33].

The first ingredient is the monodisperse RDF. Onishi & Seifert [25] propose the empirically fitted form

$$g_{ii}(R) - 1 = \begin{cases} A_1 St^2 & \text{for } St_i < St_a \\ A_2 Re_\lambda St^{-2} & \text{for } St_a \leq St_i, \end{cases} \quad (6)$$

where  $A_1 = 110$ ,  $A_2 = 0.38$  and  $St_a = ((A_2/A_1)Re_\lambda)^{1/4}$  (the full formulation is given in Appendix A). The explicit dependence on  $Re_\lambda$  is intended to capture the influence of internal intermittency on preferential concentration at increasing Reynolds numbers. For  $St_i < St_a$ , the model predicts that clustering is essentially independent of  $Re_\lambda$ , recovering the scaling  $g_{ii}(R) - 1 \propto St_i^2$ , which is consistent with the leading-order small- $St_i$  result of Wang et al. [33].

The second ingredient is the extension to droplets of unequal inertia, since droplets with different Stokes numbers need not cluster in the same regions of space. Onishi et al. use the formulation of Zhou et al. [10] to express the bidisperse RDF in terms of the monodisperse value of each species as

$$g_{ij}(R) = 1 + \rho_{ij}[(g_{ii}(R) - 1)(g_{jj}(R) - 1)]^{1/2}. \quad (7)$$

Here,  $\rho_{ij}$  is a correlation coefficient quantifying the spatial overlap between the droplet clusters of species  $i$  and  $j$ . By construction,  $0 \leq \rho_{ij} \leq 1$ : values near unity correspond to strong overlap, whereas  $\rho_{ij} \rightarrow 0$  indicates that the two clustering patterns are effectively decorrelated. The key assumption of Zhou et al. is that, to leading order, this overlap is determined solely by the Stokes-number ratio and is symmetric under exchange of the two species. Defining  $\phi = \max(St_i/St_j, St_j/St_i)$ , they therefore represent the correlation coefficient by a single function  $\rho(\phi)$ . Fitting separately in the ranges  $1 \leq \phi \leq 2.5$  and  $\phi > 2.5$  to DNS data at  $Re_\lambda = 45$ , and combining the resulting expressions with a tanh-based smoothing function, they obtain

$$\rho_{ij} = 2.6 \exp(-\phi) + 0.205 \exp(-0.0206\phi) \frac{1}{2} [1 + \tanh(\phi - 3)]. \quad (8)$$

Finally, Onishi and coauthors adopt the model of Wang et al. [33] to evaluate the RRV. In this framework,  $\langle w_r \rangle$  is composed of a shear-induced and an acceleration-induced contribution,  $\langle w_r \rangle^2 = \frac{2}{\pi} (w_{\text{shear}}^2 + w_{\text{accel}}^2)$ , a separation also adopted in more recent models (see Ref. [32] for a review), where differential sampling in polydisperse suspensions contributes primarily through the acceleration term. The model was formulated and validated at  $Re_\lambda \leq 75$ . Explicit expressions for  $w_{\text{shear}}$  and  $w_{\text{accel}}$  following Wang et al. [33] are given in Appendix B.

## III. METHODS

We consider inertial particles suspended in three-dimensional homogeneous isotropic turbulence. The flow velocity field  $\mathbf{u}(\mathbf{x}, t)$  is the solution of the incompressible Navier-Stokes equations. We assume that particles are small ( $r \ll \eta$ , where  $\eta = (\nu^3/\varepsilon)^{1/4}$  is the Kolmogorov length scale) and heavy compared to the carrier gas ( $\rho_p/\rho_f = 800$ ). Under these conditions, particles neither disturb the flow nor experience significant hydrodynamic interactions, so their motion can be described by the point-particle approximation

$$\dot{\mathbf{x}} = \mathbf{v}, \quad \dot{\mathbf{v}} = \frac{\mathbf{u}(\mathbf{x}, t) - \mathbf{v}}{\tau_p} + \mathbf{g}. \quad (9)$$

Here,  $\mathbf{x}(t)$  and  $\mathbf{v}(\mathbf{x}(t), t)$  are the Lagrangian particle position and velocity, respectively, and  $\mathbf{g} = -g\mathbf{e}_z$  is the gravitational acceleration. The point-particle approach is justified for atmospheric clouds, where typical droplet volume fractions  $\Phi_p = \frac{1}{V} \sum_{i=1}^{N_p} \frac{4}{3} \pi r_i^3$  are on the order of  $\mathcal{O}(\Phi_p) = 10^{-6}$  [2]. Throughout this work, we will use the terms ‘‘particle’’ and ‘‘droplet’’ interchangeably.

We utilize isotropic homogeneous turbulent flow fields obtained from an in-house solver ( $Re_\lambda = 55$  and 179) as well as from the Johns Hopkins Turbulence Database [34] (JHTDB,  $Re_\lambda = 418$ ). The fields are generated by solving the incompressible Navier-Stokes equations using a pseudo-spectral method with low-wavenumber forcing. In all cases,

TABLE I. Summary of flow characteristics and computational parameters.

Case	M	$Re_\lambda$	$\nu$	$\eta$	$\tau_\eta$
In-house-256	256	55	0.0075	0.039	0.2006
In-house-512	512	179	0.008	0.007	0.0613
JHTDB [34]	1024	418	0.000185	0.0028	0.0424

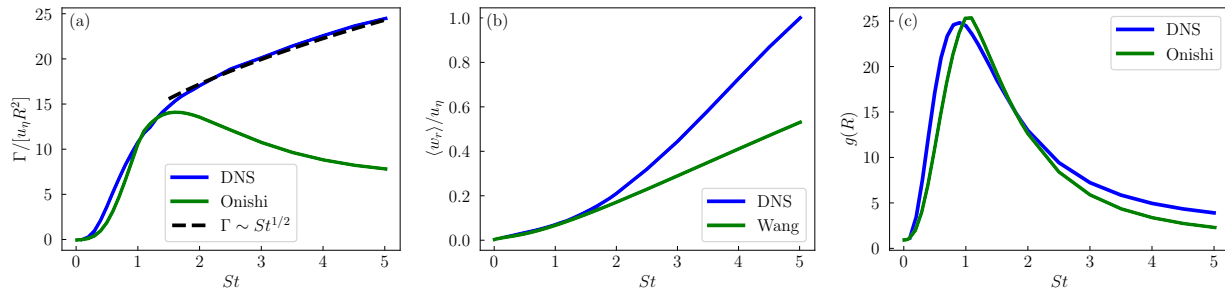


FIG. 1. Comparison of monodisperse statistics at  $Re_\lambda = 418$ : (a) collision kernel, (b) radial relative velocity (RRV) and (c) radial distribution function (RDF) at contact as a function of the Stokes number. DNS results (blue), are compared against model expressions (green). Note that the Wang model [33] was originally validated against  $Re_\lambda \leq 75$  DNS data.

the computational domain consists of a periodic cube of side length  $L = 2\pi$ , discretized into  $M$  grid points. The flow characteristics and simulation parameters are given in Table I.

Equation (9) is solved for large ensembles of particles by trilinearly interpolating the flow velocity to the particle positions and using an integration scheme adapted from Jenny et al. [35]. We use an in-house parallel solver designed to run on massively parallel compute architectures. The computational domain is decomposed into pencils, and particles are distributed across mpi [36] ranks. Despite the point-particle approximation, a mass  $m$  is assigned to every particle, thereby defining the radius  $r = (3m/(4\pi\rho_p))^{1/3}$  and, through Eq. (1), the relaxation time  $\tau_p$ . Gravitational settling is neglected ( $g = 0$ ) in most of our simulations, except for those discussed in Secs. IV B 3 and IV C.

Collision statistics are computed using the ghost-collision approach, where particles pass through each other without interaction. We determine the (dynamic) collision rate by counting the number of pairs per unit time satisfying the contact condition  $|\Delta\mathbf{x}| \leq R$ . To count efficiently, a binary tree data structure is constructed on each rank during every time step, and particles close to boundaries are exchanged with the neighboring ranks to check for inter-rank collisions. Spherical shells of thickness  $s = 0.1R$  are used to obtain consistent results for the RRV and RDF (see Ref. [33]), and the results are averaged over ensembles of  $N \geq 10^8$  particles. It was verified that the dynamic matches the kinematic collision kernel within statistical uncertainty.

To obtain the statistics presented in Secs. IV A and IV B, we initialize  $N_p = 5 \cdot 10^8$  particles per Stokes number uniformly at random in the domain. Precursor simulations are performed for a time  $t_0 = 165\tau_\eta$  to reach statistical stationarity of the collision rate. The simulations are then restarted from  $t_0$  and the ghost collision algorithm is used to detect collisions. When clustering is strong, colliding particles tend to stay together for multiple time steps or come into contact again later in time. To avoid overestimation of the collision rate in these cases (specifically for monodisperse suspensions), the results collected during the first ten time steps are discarded to exclude repeated contacts between particles that had already collided at times  $t < t_0$ . Each pair is only allowed to collide once. Particle trajectories are linearly extrapolated to detect in-between-time step collisions.

For the simulations with coalescence, we assume a collision efficiency of one. This means that each colliding particle pair  $(i, j)$  is replaced by a new particle introduced at the position  $\mathbf{x}_{\text{new}} = (m_i\mathbf{x}_i + m_j\mathbf{x}_j)/(m_i + m_j)$  with mass  $m_{\text{new}} = m_i + m_j$  and velocity  $\mathbf{v}_{\text{new}} = (m_i\mathbf{v}_i + m_j\mathbf{v}_j)/(m_i + m_j)$ . The number of initialized particles varies across runs (as documented in Table II) in order to keep the volume fraction  $\Phi_p = 8.5 \cdot 10^{-6}$  constant. Particles that initially overlap with others are removed from the simulation.

## IV. RESULTS

### A. Monodisperse suspensions

The collision statistics for the monodisperse case are shown in Fig. 1. In panel (a), the collision kernels obtained from the DNS (blue) and from the model expressions (green) are plotted as a function of the Stokes number. Following Refs. [26, 37], we normalize the collision kernel by  $R^2 u_\eta$ . Gravitational settling is neglected. The collision kernel increases rapidly with the Stokes number, most notably in the range  $0.3 \leq St \leq 1$ . At larger  $St$ , the collision kernel scales as  $\Gamma \sim St^{1/2}$ , as shown by the dashed black line. The dependence of the collision kernel on the Stokes number can be understood by examining the two terms appearing in Eq. (3): the RRV and the RDF at contact, shown in Figs. 1(b) and (c), respectively. The growth of  $\langle w_r \rangle$  is gentle and approximately linear at first, but increases more rapidly at larger  $St$ . This behavior is attributed to the sling effect, which becomes increasingly biases the relative velocity statistics between same-sized particles at contact. The RDF, on the other hand, is notably non-monotonic. Particles disperse homogeneously in space with  $St \rightarrow 0$  and  $St \rightarrow \infty$ , respectively, resulting in  $g(R) = 1$  in both limits. In between, the RDF peaks at  $St \approx 1$ , commonly identified as the Stokes number with maximum clustering. The dependence of  $\Gamma$  on the  $St$  can thence be interpreted as the combined effect of  $\langle w_r \rangle$  and  $g(R)$ . It is tempting to attribute the steep increase of the collision kernel between  $St \approx 0.3$  and  $St \approx 1$  solely to preferential concentration, since the RDF grows at a slope far greater than that of the RRV. However, separating preferential concentration and the sling effect in this manner is not possible, since caustics are also involved in facilitating clustering [29]. A study by Vosskuhle et al. [37] showed that the sling effect already significantly contributes to the collision dynamics at  $St \gtrsim 0.75$ , yet the ensemble-averaged RRV only weakly affects the product  $\langle w_r \rangle g(R)$  in this range.

While preferential concentration decreases with Stokes numbers exceeding  $St = 1$ , the RRV continues to grow. Beyond  $St \gtrsim 2$ , our data suggest a scaling of the collision kernel proportional to  $St^{1/2}$ . This scaling is consistent with theoretical predictions [38, 39] of the RRV in the sling-dominated regime at high Reynolds numbers, where particle velocities become increasingly uncorrelated with both the instantaneous flow field and with those of nearby particles. In this regime, particle velocities are randomly distributed, making a gas-kinetic approach following Abrahamson [40] more appropriate. It has been suggested that the collision kernel should be expressed as the sum  $\Gamma = \Gamma_{\text{adv}} + \Gamma_{\text{sling}}$ , explicitly differentiating between the collision of particles that experience caustics and those that do not [37, 38].

The Onishi model provides a remarkably good estimate for the monodisperse RDF, especially considering that the model was used “out-of-the-box”, without re-fitting the parameters to our DNS data. The Wang model, on the other hand, underestimates  $\langle w_r \rangle$  for  $St \gtrsim 1.5$ , i.e., it does not accurately capture the enhanced relative motion of heavier particles due to the sling effect. As a result, the combined expression for the monodisperse collision kernel agrees well with the DNS data for  $St \lesssim 1.5$ , but fails to reproduce the  $\Gamma \sim St^{1/2}$  scaling at larger  $St$ .

### B. Bidisperse suspensions

Now, how does polydispersity, naturally occurring in cloud droplet populations, affect the collision dynamics? To address this question, we compute the collision kernel, RRV and RDF at contact for non-settling droplet pairs  $(i, j)$  with Stokes numbers ranging from  $St = 0.02$  to  $St = 2$ . The results are shown in the top row of Fig. 2 as pseudocolor matrices mapped across Stokes number pairs, while the bottom row shows the corresponding model predictions. The complete map of the collision kernel is provided in Table III for future reference.

In agreement with the monodisperse results, the collision rate generally increases with the Stokes number, resulting from the combined effects of  $\langle w_r \rangle$  and  $g(R)$ . We observe that the RRV increases with the Stokes number separation within the colliding pair, and that  $\langle w_r \rangle_{ij} \geq \max(\langle w_r \rangle_{ii}, \langle w_r \rangle_{jj})$ . The enhancement of the RRV due to differential sampling largely outweighs its increase along the diagonal. Conversely, the RDF peaks along the diagonal and quickly drops as the Stokes numbers separate. This is indicative of the rapid decorrelation of the particle clusters due to differential sampling.

We observe that the behavior of the bidisperse kernel falls into two regimes. At small Stokes numbers (i.e., when both  $St_i, St_j \lesssim 0.4$ ), polydispersity enhances collisions even when it reduces the Stokes number of one of the colliding droplets. This behavior is evident in Fig. 2(a): starting from a point on the diagonal ( $St_i, St_j \leq 0.4$ ), moving horizontally to the left or vertically downward—thus decreasing one Stokes number while keeping the other fixed—results in an increase in  $\Gamma$ . To explain this behavior, consider the competing effects of polydispersity to decrease particle clustering yet increase relative motion. At small Stokes numbers, particles tend not to detach from the flow, and preferential concentration is weak. As a result, the enhancement of the relative velocities due to differential sampling is more significant, and the net effect of polydispersity on the collision kernel is positive. Conversely, at larger Stokes numbers,  $St \gtrsim 0.4$ , preferential concentration significantly contributes to the collision rate, and the loss of clustering due to polydispersity outweighs the increase in relative velocities, leading to an attenuation of collisions.

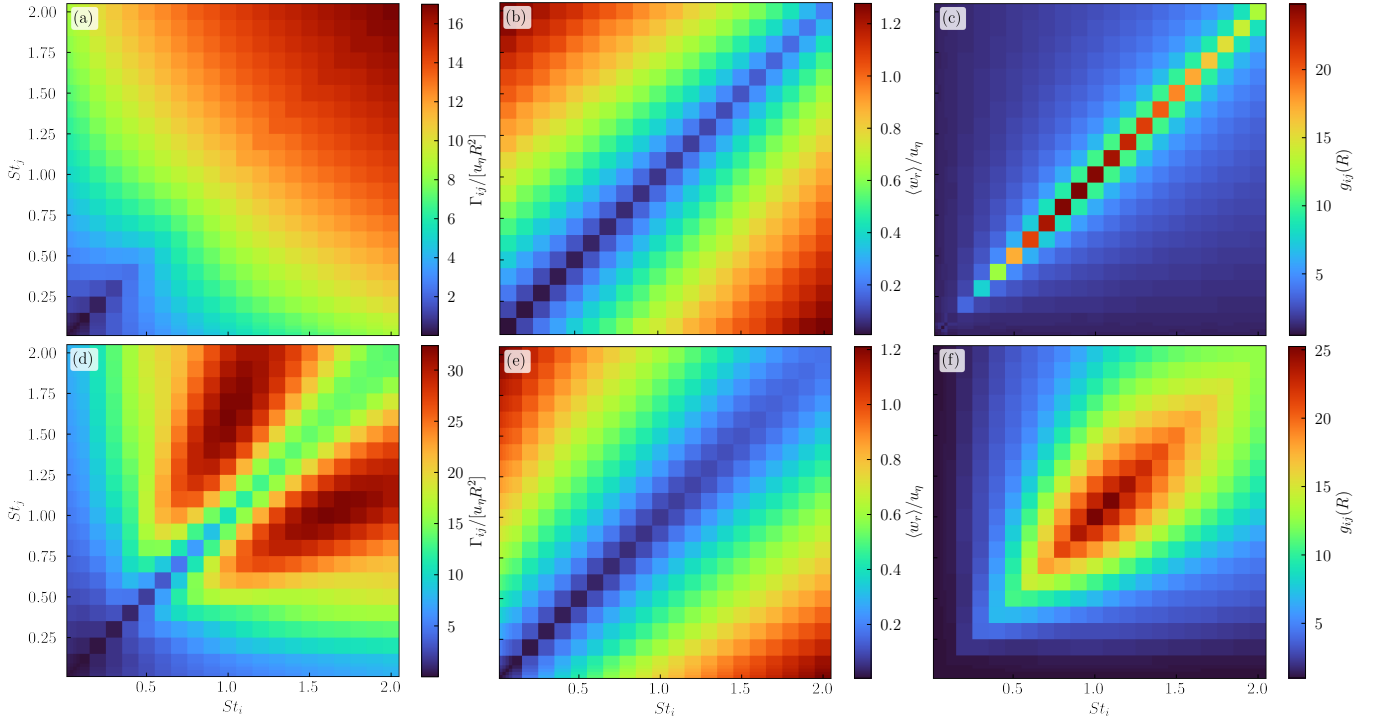


FIG. 2. Bidisperse collision statistics for droplet pairs  $(St_i, St_j)$ : (a-c) DNS results at  $Re_\lambda = 418$  (top row) compared with (d-f) predictions from Onishi/Wang model [25, 33] (bottom row). Columns represent the (a,d) collision kernel, (b,e) RRV and (c,f) RDF at contact, respectively.

In this regime, the collision kernel increases only when one of the Stokes numbers—and thus the overall inertia of the droplet pair—becomes larger.

James & Ray [8] have reported bidisperse collision kernels obtained from DNS of two-dimensional particle-laden turbulence. Their data show a pronounced increase in the collision rate along the diagonal, indicating that collisions between same-sized particles are strongly enhanced. Our results do not exhibit this behavior; instead, the collision kernel varies smoothly with the Stokes number separation. In preparing this paper, we identified that this discrepancy may arise from the algorithm used to detect collisions. In monodisperse suspensions, colliding droplet pairs can remain in contact over prolonged periods of time or re-enter contact later, leading to an overestimation of the collision rate, particularly under conditions of strong clustering. To mitigate this effect, the first ten time steps of the detection procedure are discarded, and each droplet pair is allowed to collide only once, as described in Sec. III. More fundamentally, the use of two-dimensional turbulence limits the applicability of their results to atmospheric conditions. The distinct characteristics of 2D turbulence, such as the inverse energy cascade, may not accurately capture the collision dynamics relevant to cloud droplets. Two-dimensional turbulence lacks the flow structures and intermittency associated with three-dimensional turbulence, which are possibly crucial for the collision dynamics of cloud droplets. For example, it has been demonstrated [13, 14] that caustic formation occurs through specific flow topologies specific to three-dimensional turbulence. Moreover, Onishi & Vassilicos [23] compared the collision statistics in 2D and 3D DNS and found that inertial clustering is reduced with increasing  $Re_\lambda$  due to internal intermittency, absent in 2D turbulence.

Figure 2(d) shows the collision kernel obtained from the Onishi model, with the corresponding expressions for  $\langle w_r \rangle$  (Wang model, see Sec. B) and  $g_{ij}(R)$  (Eqs. (6-8)) shown in Figs. 2(e) and (f), respectively. We find that the Wang model captures the qualitative trends of the bidisperse RRV. For  $St < 1.0$ ,  $\langle w_r \rangle$  agrees with the DNS results to within 10%. Larger errors are observed mainly for differently-sized particles at larger Stokes numbers, for which the Wang model underestimates the relative velocities due to differential sampling. The bidisperse RDF, on the other hand, is not estimated accurately by the Zhou model. The DNS data display a more rapid decorrelation of the droplet clusters compared to the predictions provided by Eq. (8). As a result, the Onishi model strongly overestimates the bidisperse collision kernel, specifically for droplet pairs with Stokes numbers  $St_i, St_j > 1$ . The relative error with respect to the DNS data of the Onishi model is shown in Fig. 4(d).

### 1. Bidisperse correlation coefficient

Comparing Figs. 2(c) and (f) shows that the Zhou model [10] overestimates bidisperse clustering, indicating that the correlation coefficient  $\rho(\phi)$  prescribed by Eq. (8) decays too slowly with increasing  $\phi = \max(St_i/St_j, St_j/St_i)$ . Indeed, we find that the droplet clusters decorrelate faster than the model suggests. This is apparent in Fig. 3(a), which shows the correlation coefficient  $\rho_{ij} = (g_{ij}(R) - 1)/[(g_{ii}(R) - 1)(g_{jj}(R) - 1)]^{1/2}$  obtained from the DNS as a function of  $St_i/St_j$  alongside the prediction from Eq. (8). Here, we show droplet pairs with Stokes numbers in the range  $St \in [0.2, 2.0]$ , since clustering is very weak for  $St \geq 0.2$ , even in the monodisperse case. We find that our data collapse quite well, for all simulated Reynolds numbers. The Zhou model, however, exhibits systematic discrepancies relative to the DNS data. In addition, we find that the correlation coefficient is not quite symmetric around  $St_i/St_j = 1$ , suggesting that the assumption fundamental to the derivation of Zhou et al. [10] is physically unjustified.

We now provide arguments to explain the observed behavior. First, we ask why the Zhou model systematically overestimates the bidisperse overlap. Ayala et al. [32] observed similar errors but concluded they were a consequence of neglecting gravity in the model’s derivation. In contrast, the present work demonstrates that the model remains inaccurate even for non-settling droplets. Since the Zhou model was derived at a relatively low  $Re_\lambda = 45$ , it is tempting to assume that the observed discrepancies stem from the larger Reynolds numbers used in this work. Somewhat unexpectedly, however, our data for all three simulated  $Re_\lambda = 55, 179$  and  $418$  collapse quite well, suggesting that  $Re_\lambda$  is not the primary driver of the error. While the lowest Reynolds number case ( $Re_\lambda = 55$ ) deviates slightly from the trend—potentially because a narrow inertial subrange may cause clustering length scales to overlap with energy-containing scales—this remains a minor effect. Instead, we propose that the discrepancy may be an artifact of the “frozen” flow field (i.e., advecting particles through a static velocity field) used in the original derivation. A previous study [41] indicated that this approach can lead to an overestimation of particle clustering. While we do not verify this directly here, it stands as the most plausible explanation for the model’s systematic failure to reproduce the current DNS results.

Note that the cross-species correlation coefficient is symmetric, i.e.,  $\rho(St_i, St_j) = \rho(St_j, St_i)$ . The apparent asymmetry around  $St_i/St_j = 1$  in Fig. 3(a) arises because  $\rho$  is plotted as a function of  $St_i/St_j$  while  $St_j$  is held fixed. For  $St_i < 1$ , decreasing  $St_i$  approaches the tracer limit, leading to a faster decay of the cross-correlation. The asymmetry  $\rho(St_i/St_j) \neq \rho(St_j/St_i)$  motivates the use of an alternative parameter to replace  $\phi = \max(St_i/St_j, St_j/St_i)$  in modeling the correlation coefficient. The dispersion parameter

$$\theta_{ij} = \frac{St_i - St_j}{St_i + St_j} \quad (10)$$

provides a suitable alternative, as the collision statistics are naturally symmetric with  $\theta_{ij} = -\theta_{ji}$ , so that the modeling task reduces to finding an expression for  $\rho(\theta)$ , where  $\theta = |\theta_{ij}|$ . Moreover, the dispersion parameter offers a quantification of the  $St$ -separation *relative* to the overall inertia of the droplet pair. Based on this reasoning, we expect  $\rho(\theta)$  to exhibit a more universal behavior compared to  $\rho(\phi)$ , which Fig. 3(b) confirms in the affirmative. The majority of data points collapse on an exponential curve, so that

$$\rho(\theta) = 0.77 \exp(-27.9\theta) + 1.96 \exp(-4.67\theta)^{\frac{1}{2}} [1 + \tanh(\theta - 1)] \quad (11)$$

provides an excellent fit to the DNS data. To obtain this expression, we used the composite formulation from the Zhou model and performed a least-squares fit on the  $Re_\lambda = 179$  and  $418$  DNS data. In general, we conclude that our formulation improves the predictions of the bidisperse correlation coefficient in the absence of gravity, while exhibiting negligible sensitivity to  $Re_\lambda$ .

### 2. A novel parameterization for the bidisperse collision kernel

In the previous section, we showed that although the Onishi model accurately predicts monodisperse clustering, it produces large errors in the bidisperse case, as evident from Fig. 4(d). This limitation arises from its reliance on the Zhou model, which fails to capture the rapid decorrelation of particle clusters as  $St_i$  and  $St_j$  diverge. Having introduced an improved version of this model (Eq. (11)), we now move on to present a compact parameterization for the bidisperse collision kernel as a function of the dispersion parameter,  $\theta$ . This is motivated by the observation that the kernel varies smoothly as the Stokes numbers separate, whereas both the RDF and RRV do not. Letting  $\tau = St_i + St_j$  and  $\delta = St_i - St_j$ , we consider the first-order approximation  $\Gamma(\tau, \delta) = \Gamma(\tau, 0) + E(\tau) \frac{\delta}{\tau} + \mathcal{O}(\delta^2)$ . Here, the sign and magnitude of the polydisperse “enhancement factor”  $E(\tau)$  depend on the overall inertia  $\tau$ , but not on the separation  $\delta$ . As established earlier, the effect of polydispersity arises from the competition between increased relative

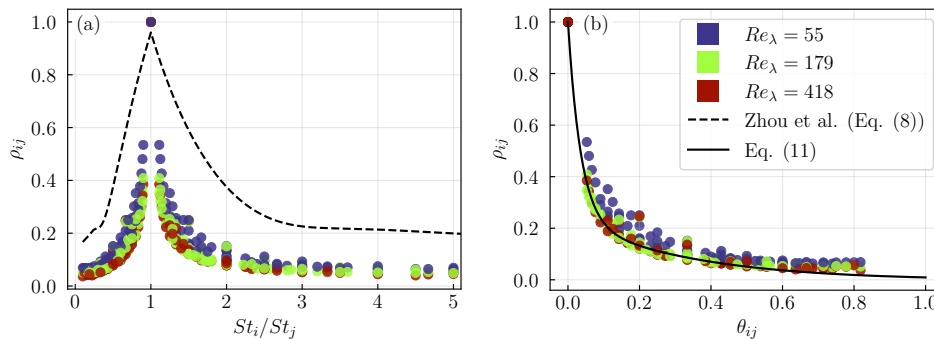


FIG. 3. Evaluation of bidisperse clustering: (a) Cross-species correlation coefficient versus Stokes number ratio obtained from the DNS at  $Re_\lambda = 55, 179$  and  $418$  ( $St \in [0.2, 2.0]$ ) and with the Zhou model (Eq. (8), originally validated at  $Re_\lambda = 45$ , black dashed line). (b) The same data plotted against the dispersion parameter,  $\theta_{ij}$ , together with the prediction from Eq. (11) (black solid line).

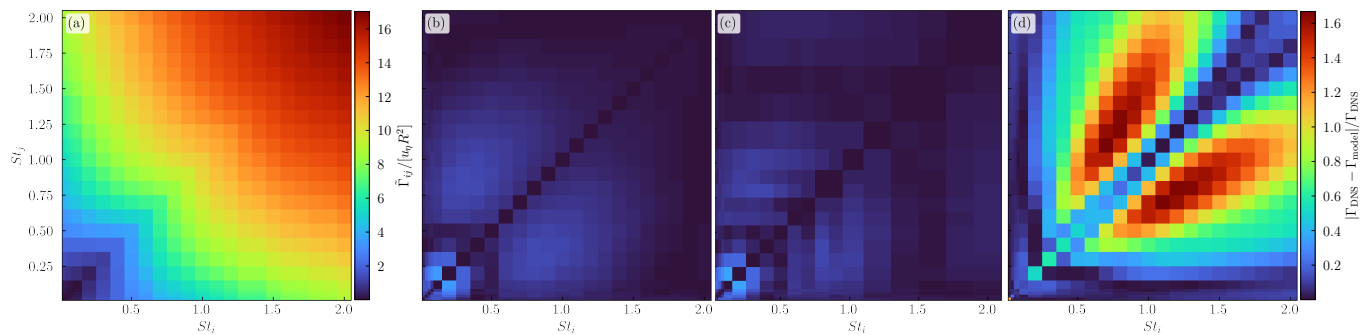


FIG. 4. Validation of the proposed parameterization (Eq. (12)): (a) Predicted kernel matrix using DNS-derived  $\Gamma_{ii}$  and  $\Gamma_{0i}$  ( $St_0 = 0.02$ ) at  $Re_\lambda = 418$ . Relative error of the parameterization with respect to the DNS at (b)  $Re_\lambda = 418$  and (c)  $Re_\lambda = 179$ , compared to (d) the error obtained from the Onishi/Zhou model. A common color scale is used for panels (b-d).

velocities and reduced preferential concentration as  $St_i$  and  $St_j$  diverge. To quantify this balance, we seek a reference quantity that isolates the velocity enhancement from spatial correlations. On the basis of empirical observations, we find that the kernel  $\Gamma_{0i}$ , describing interactions between tracer-like droplets ( $St_0 \ll 1$ ) and droplets with  $St_i$ , provides a suitable measure, as it primarily captures the contribution from differential sampling. Hence, the net enhancement due to polydispersity is approximated by the difference  $E(\tau) = \Gamma_{0i} - \Gamma_{ii}$ .

Following this approach, we find that the bidisperse collision kernel for a droplet pair  $(i, j)$  with  $St_i \geq St_j$  can be effectively parameterized as

$$\tilde{\Gamma}_{ij} = \theta_{ij}\Gamma_{0i} + (1 - \theta_{ij})\Gamma_{ii}. \quad (12)$$

Here,  $\Gamma_{ii}$  is the monodisperse collision kernel and  $\Gamma_{0i}$  is the collision kernel between particles of  $St_i$  and very light, close-to-tracer particles (shown in Fig. 5 with  $St_0 = 0.02$ ). Note that  $\Gamma_{ii}$  corresponds to the diagonal and  $\Gamma_{0i}$  to the bottom row (or first column) of Fig. 2(a). The parameterization is given for  $St_i \geq St_j$  so that  $\theta_{ij} \geq 0$ , but extension to arbitrary pairs follows directly from symmetry. The heuristic behind expression (12) is the separation of the collision kernel into inertial effects (preferential concentration and the sling effect, represented by the monodisperse kernel) and differential sampling (represented by  $\Gamma_{0i}$ ). The resulting bidisperse kernel blends the two contributions, weighted by the dispersion parameter  $\theta_{ij}$ . One easily verifies that as  $St_j \rightarrow 0$ , the correct asymptotic behavior  $\tilde{\Gamma}_{ij} = \Gamma_{0i}$  is recovered. Similarly, for  $i = j$ , Eq. (12) simplifies to the monodisperse collision kernel.

Figure 4(a) displays the predictions of Eq. (12), allowing direct comparison to the DNS reference (Fig. 2(a)). The compact linear formulation captures the effect of differential sampling on the collision kernel with remarkable qualitative accuracy. It reproduces the enhancement due to polydispersity at small Stokes numbers, even when the mean Stokes number of the colliding pair is reduced. This behavior arises because initially,  $\Gamma_{0i}$  increases more rapidly with  $St_i$  through differential sampling than  $\Gamma_{ii}$  increases through inertial effects, leading to  $\Gamma_{0i} > \Gamma_{ii}$  for small  $St_i$  and  $\Gamma_{ii} > \Gamma_{0i}$  for  $St_i \gtrsim 0.4$ .

Figures 4(b,c) show the relative errors of our model with respect to the DNS data at  $Re_\lambda = 418$  and  $Re_\lambda = 179$ ,

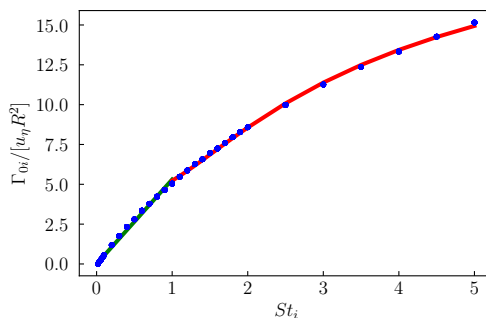


FIG. 5.  $\Gamma_{0i}$  obtained from the DNS at  $Re_\lambda = 418$  with  $St_0 = 0.02$  (blue dots). The green and red lines depict the empirical fits  $\Gamma_{0i} = aSt_i$  with  $a = 5.3$  and  $\Gamma_{0i} = b_0 + b_1 \exp(-b_2/St_i)$  with  $b_0 = 4.3$ ,  $b_1 = 19.6$ ,  $b_2 = 3.05$ , respectively.

respectively. For both Reynolds numbers, the predictions generally agree with the DNS results to within 10%. Larger errors are seen primarily for small Stokes numbers around the diagonal, since the collision kernel is near zero in this region, thus amplifying the relative error signal. Overall, the predictions of our parameterization fit the DNS data significantly better than the Onishi/Zhou model, whose relative error is shown in Fig. 4(d). The Onishi/Zhou predictions deviate most strongly for off-diagonal pairs with  $St \gtrsim 1$ , where the overestimation of the bidisperse correlation coefficient with Eq. (8) is most pronounced.

Recall that  $\Gamma_{0i}$  describes the collisions between droplets with  $St_0 \ll 1$  (tracer-like) and  $St_i$ . In order for Eq. (12) to yield a complete model for the bidisperse collision kernel, an explicit expression for  $\Gamma_{0i}$  is required (whereas  $\Gamma_{ii}$  can be modeled with the Onishi model). In this regime, preferential concentration is negligible ( $g_{i0}(R) \approx 1$  for sufficiently small  $St_0$ ), and the collision dynamics are dominated by the RRV. James & Ray [8] derived analytical expressions for  $\langle w_r \rangle$  under various limiting assumptions. They demonstrate that with  $St_j \ll 1$ , the RRV obeys the linear scaling  $w_r \sim St_i$  if  $St_i \lesssim 1$  and exponential scaling of the form  $w_r \sim \exp(-1/St_i)$  for  $St_i \gg 1$ . Since  $g(R) \approx 1$  in this regime, we can translate the scaling of the RRV to the collision kernel. In Fig. 5, we show the  $\Gamma_{0i}$  kernel obtained using  $St_0 = 0.02$  and apply the two scaling laws. The DNS data are well described by these fits.

### 3. Influence of gravitational settling

Because this work is primarily concerned with the role of turbulence in enhancing collisions between cloud droplets, gravity has been neglected in the simulations discussed thus far. While these results have specific relevance to the warm rain context—particularly for small droplets ( $r \approx 10\mu\text{m}$ ) that encounter intermittent high-dissipation events—their direct applicability to the onset of precipitation is limited. Under mean-field conditions, and as droplets grow beyond  $r \approx 15\mu\text{m}$ , gravitational settling becomes an important factor in the collision-coalescence process [2, 42]. To assess the robustness of our parameterization for settling droplets, we performed additional DNS including gravity. A uniform gravitational acceleration  $g$  is applied along the negative  $z$ -direction. The Froude number is set to  $Fr = \varepsilon^{3/4}/(\nu^{1/4}g) = 0.173$ , representative of a cumulus cloud with  $\varepsilon = 0.05\text{ m}^2/\text{s}^3$ . With Stokes numbers spanning  $St \in [0.02, 2]$ , the settling parameters range from  $Sv = St/Fr \approx 0.12$  to 11.6. Note that this corresponds to cloud droplet radii of approximately  $r \in [5.4, 54]\mu\text{m}$ .

Figure 6(a) displays the ratio between the settling and non-settling collision kernel, mapped across Stokes number pairs. In this figure, the droplet radius (and thus  $Sv$ ) is varied, but we use the Stokes number to keep the visualizations consistent with the preceding sections. Collisions between same-sized droplets (along the diagonal) are attenuated by settling. This result is consistent with earlier monodisperse studies [43]. Physically, gravity advects droplets through the coherent flow structures on timescales shorter than the local eddy turnover time, thereby reducing the residence time available for accumulation in strain-dominated regions. This weakened interaction between the droplets and the flow manifests itself in attenuated preferential concentration and fewer sling events. As a result, both the RDF and the RRV are reduced for monodisperse droplets compared to the non-settling case, and the collision rate is lower. Away from the diagonal, however, the picture reverses. Droplets of different sizes settle at different terminal velocities, adding a systematic contribution to the relative velocity that grows with size separation. This mechanism strongly enhances collisions, so that the off-diagonal entries of the kernel matrix increase substantially relative to the zero-gravity case.

A key question is whether the parameterization for the bidisperse collision kernel derived in the absence of gravity (Eq. (12)) remains valid for settling droplets, for which differential settling is the dominant collision mechanism at

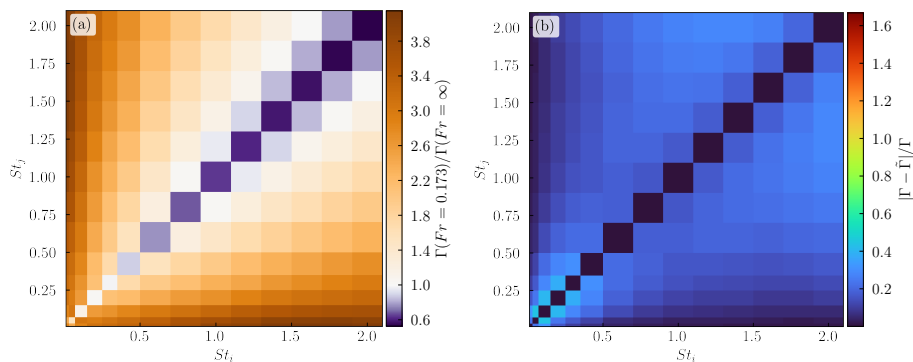


FIG. 6. Influence of gravity on bidisperse collisions: (a) Ratio between settling ( $Fr = 0.173$ ) and non-settling collision kernels and (b) relative errors incurred by our parameterization (Eq. (12)). Note that the color scale of panel (a) is asymmetric. The color scale in panel (b) is identical to that used in Figs. 4(b-d).

large size separations. Our data suggest that it does: Figure 6(b) shows the relative error of our model against the DNS at  $Fr = 0.173$ . The errors are generally larger compared to the non-settling case, yet the parameterization continues to reproduce the full bidisperse kernel qualitatively across the majority of the parameter space. This confirms that the underlying structure of the model—a linear blend between the monodisperse and polydisperse effects weighted by  $\theta$ —captures the essential physics even when differential settling is the dominant source of relative motion. In the presence of gravity, we find that  $\Gamma_{0i} > \Gamma_{ii}$  for all  $St_i$ , implying that the polydisperse contribution consistently exceeds the monodisperse one.

### C. Turbulent broadening of the droplet size distribution

We now shift from the ghost collision approach to simulations involving coalescing droplets. These simulations allow us to study the broadening of the droplet size distribution (DSD), without relying on the simplifying assumptions of Smoluchowski-type collision-coalescence models, which underestimate the rapid formation of lucky droplets through successive correlated collisions [44]. As discussed in the Introduction, the inertia and settling of cloud droplets vary along their trajectories because the local turbulence intensity fluctuates in space and time. Consequently, collision-coalescence is modulated by the instantaneous local dissipation rate. To study the impact of  $\varepsilon$  on droplet growth without the computational expense of additional simulations, we exploit the scaling relations  $St \propto r^2 \varepsilon^{1/2}$  and  $Sv \propto r^2 \varepsilon^{-1/4}$ . In particular, increasing the dissipation rate by a factor  $\alpha^4$  affects droplet inertia in a manner equivalent to scaling the droplet radii by  $\alpha$  while keeping the flow field unchanged (whereas the settling parameter decreases by  $1/\alpha$ ). This equivalence enables us to emulate dissipation rate fluctuations by appropriately scaling the initial DSD.

We emphasize that the simulations are performed at fixed  $Re_\lambda = 418$ , well below the realistic values in atmospheric clouds ( $\mathcal{O}(10^4)$ ). As noted in the Introduction, clustering shows a weak, yet non-negligible  $Re_\lambda$ -sensitivity, since extrapolation of the DNS to atmospheric conditions spans at least one order of magnitude. On the basis of the cited reports [24–26], we therefore expect our simulations to slightly overestimate the growth of droplets with  $0.4 \lesssim St \lesssim 1$ . At higher  $Re_\lambda$ , dissipation rate fluctuations become more intense yet more localized in space and time. While the aim of our study is to demonstrate accelerated droplet growth in highly dissipative parcels, by no means do we claim that our simulations reproduce the cloud-realistic statistics of  $\varepsilon$ .

Droplet populations are initialized with radii following a Gaussian distribution,  $r \sim \mathcal{N}(r_0, \sigma_r^2)$ , with mean  $r_0$  and standard deviation  $\sigma_r$ , as is expected to result from condensation. Both  $r_0$  and  $\sigma_r$  are scaled by  $\alpha$ , so that a shift in the local energy dissipation rate by a factor of  $\varepsilon/\varepsilon_0 = \alpha^4$  is emulated. For example, by setting  $\alpha = 1.23$ , we adjust the mean Stokes number from  $\langle St \rangle = 0.15$  to  $\langle St \rangle = 0.23$ , corresponding to a 2.28-fold increase in the local energy dissipation rate. The parameters of all cases are given in Table II. Since the droplets grow upon collision, gravitational settling must be accounted for in these simulations, and the Froude number scales with  $\alpha^3$ . To keep the droplet volume fraction  $\Phi_p \propto nr^3$  unchanged, the initial number of droplets,  $N_p(t=0)$ , is reduced as  $\alpha$  grows. A cloud-realistic value of  $\Phi_p = 8.5 \cdot 10^{-6}$  is kept constant throughout the simulation campaign.

Figure 7(a) shows the DSDs obtained for different values of  $\alpha$  after an integration time of  $t = 340\tau_p$ . Since we emulate dissipation fluctuations by altering the droplet phase rather than the flow field, the evaluation time is fixed relative to  $\tau_p$  rather than  $\tau_\eta$ . The dashed-dotted blue line shows the initial DSD, whereas the dashed lines show the

TABLE II. Computational parameters for the simulations with coalescing droplets: Scaling factor  $\alpha$ , corresponding increase in the dissipation rate, Froude number, mean Stokes number, mean settling parameter, and initial droplet count.

$\alpha$	$\varepsilon/\varepsilon_0$	$Fr$	$\langle St \rangle$	$\langle Sv \rangle$	$N_p(t=0)$
1	1	0.173	0.15	0.87	$9.3 \cdot 10^8$
1.23	2.28	0.322	0.23	0.71	$5 \cdot 10^8$
1.63	7.06	0.749	0.40	0.53	$2.1 \cdot 10^8$
2.15	21.4	1.719	0.69	0.38	$9.3 \cdot 10^7$

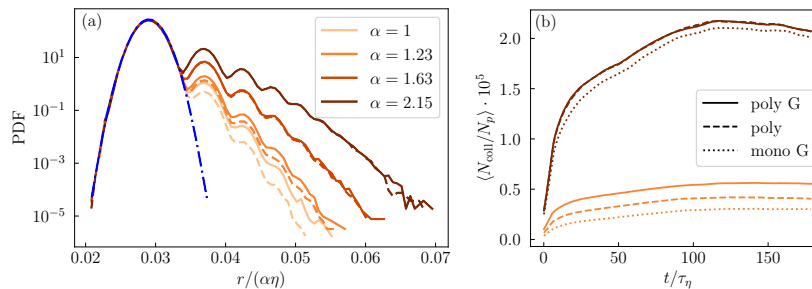


FIG. 7. DNS results for coalescing droplets. (a) Probability density functions of the droplet radii at time  $t = 340\tau_p$  for different values of  $\alpha$ . The DSD at  $t = 0$  is indicated by the blue dash-dotted line; dashed lines provide a comparison to reference cases without gravity. (b) Mean collision-coalescence count (number of collisions normalized by the total number of droplets) versus time for  $\alpha = 1.23$  and  $2.15$ . Solid lines denote the standard case with gravity, initialized with polydisperse droplet populations. For comparison, results are shown for reference simulations without gravity (dashed lines) and for a monodisperse case with gravity (dotted lines). The data are ensemble-averaged across all droplets and smoothed over intervals of  $10\tau_\eta$ .

equivalent DSDs obtained from reference runs without gravity.

All simulations are carried out in non-dimensional units. To relate these results to a physical cumulus cloud, we note that a representative Kolmogorov length scale is  $\eta \approx 0.4 \text{ mm}$  [19]. In this context, the initial droplet size corresponds to approximately  $r_0 \approx 11.6 \mu\text{m}$ , and all droplets initially have  $r < 15 \mu\text{m}$ . Despite these small radii, the droplets effectively collide and coalesce in the turbulent flow within the short simulated time interval, even in the base case ( $\alpha = 1$ ). The DSD broadens rapidly from its initial narrow Gaussian distribution, developing long tails with visibly “bumpy” profiles, owing to the narrow initial size spread combined with the discrete, binary nature of coalescence events. The long tails indicate that a few lucky droplets have grown disproportionately (note the logarithmic scale of the ordinate) from repeated collisions. Notably, growth significantly accelerates as  $\alpha$  increases, indicating that higher local turbulence intensity (as represented here) effectively enhances collision-coalescence. The most pronounced changes occur when moving from  $\alpha = 1.23$  to  $\alpha = 1.63$  and  $\alpha = 2.15$ , which correspond to increases in the mean Stokes number from  $\langle St \rangle = 0.23$  to  $0.40$  and  $0.69$ , respectively. This range marks the regime of strongest enhancement, consistent with the observations from Sec. IV A.

Gravity affects the DSD evolution primarily at smaller  $\alpha$ . For  $\alpha = 1$  and  $\alpha = 1.23$ , differential settling enhances collisions, leading to faster broadening when gravity is included. For larger  $\alpha$ , the DSDs with and without gravity become nearly indistinguishable. This suggests that while differential settling is vital for typical cloud droplets under mean-field conditions, inertial effects become the dominant driver of collision-coalescence as the local dissipation rate increases.

Figure 7(b) shows the fraction of droplets that undergo collision and coalescence as it evolves in time. Collision activity ramps up during the first stage of the simulations, and stabilizes after around  $t = 100\tau_\eta$ . Alongside the baseline simulations (solid lines), which are initialized with polydisperse populations and include gravity, we also report reference results from simulations without gravity (dashed) and from simulations initialized with monodisperse populations (dotted; gravity included). The suspensions are extremely dilute, and consequently only a minute fraction of droplets, on the order of  $10^{-6}$  to  $10^{-5}$ , undergo collision and coalescence. Nevertheless, the collision rate increases sharply with  $\alpha$ . Relative to the  $\alpha = 1.23$  case, collisions occur about 3.8 times more frequently with  $\alpha = 1.63$ , supporting the notion that intermittent events of intense turbulence can substantially accelerate droplet growth. The impact of gravity can be quantified more precisely here: We observe that differential settling enhances collision-coalescence for  $\alpha = 1.23$  by 34%, whereas its effect is negligible in the  $\alpha = 1.63$  case (dashed and solid lines coincide in Fig. 7(b)).

Finally, the data highlight the complex role of polydispersity. At lower dissipation levels ( $\alpha = 1.23$ ), polydisper-

sity enhances droplet growth substantially, yielding roughly 2.2 times more collisions compared to the corresponding monodisperse simulation. This enhancement, however, weakens as the importance of droplet inertia increases, reflecting our findings from Sec. IV B, and because gravitational settling becomes relatively less important. For  $\alpha = 1.63$ , collision-coalescence in the polydisperse case exceeds that in the monodisperse reference by only about 3%.

## V. CONCLUSION

We have studied polydisperse droplet collisions in homogeneous isotropic turbulence at Reynolds numbers up to  $Re_\lambda = 418$  by means of direct numerical simulations (DNSs). The bidisperse collision kernel, relative radial velocity (RRV) and radial distribution function (RDF) at contact have been obtained for droplet pairs with Stokes numbers in the range  $St \in [0.02, 2]$ . These data are important for understanding how turbulence affects the growth of droplets in warm atmospheric clouds. The statistics were obtained in the absence of gravity, in order to isolate turbulent mechanisms and to target the smallest droplets within the bottleneck range. While these results are particularly relevant in the context of recent theories of warm rain formation that invoke turbulent intermittency and rapid growth of statistically “lucky” droplets, it is important to bear in mind that they cannot be used directly in large-eddy simulations (LESs) of convective clouds without accounting for gravitational settling of larger droplets.

Our findings establish that differential sampling is an effective mechanism by which differently-sized droplets collide under turbulence, even in the absence of gravity. This contrasts with the conventional view that primarily links polydispersity to collisions induced by gravitational settling. Droplets with separate relaxation times cluster less, but exhibit larger relative velocities, so that the influence of polydispersity is highly dependent on the Stokes number. At  $St \lesssim 0.4$ , polydispersity enhances collisions because the increased relative velocities from differential sampling compensate for the reduction in clustering. Conversely, at larger Stokes numbers, preferential concentration and the sling effect are the dominant collision mechanisms, and polydispersity attenuates collisions in this regime because it rapidly decorrelates the number density fields. Thus, the role of polydispersity transitions from enhancing to suppressing collisions as droplet inertia increases.

We have compared our DNS data to the Onishi model [25] and found good agreement for the monodisperse collision kernel up to  $St \approx 1.5$ . In contrast, the Zhou model [10], providing an expression for the spatial correlation between differently-sized droplets, was shown to introduce systematic errors in the bidisperse RDF, since it overestimates the overlap of the droplet clusters as the Stokes numbers separate. This mismatch was observed for all simulated Reynolds numbers ( $Re_\lambda = 55, 179$  and  $418$ ), and may originate from the use of frozen flow fields in the original study. Furthermore, we found that the dispersion parameter  $\theta$  (as defined in Eq. (10)) is a better choice to model the correlation coefficient, and we provided a modified expression (Eq. (11)) that fits the DNS data well across all Reynolds numbers.

We have introduced a new compact expression for the bidisperse collision kernel. This parameterization originates from the observation that, although the underlying bidisperse RRV and RDF display difficult-to-model variability with respect to  $St_i$  and  $St_j$ , the collision kernel in itself varies smoothly with the Stokes number separation. By exploiting symmetries and identifying the dispersion parameter  $\theta$  as the relevant measure, our model results from a first-order approximation that reproduces the DNS reference with high accuracy and remains robust across Reynolds numbers. Although differential settling strongly impacts polydisperse collisions in the presence of gravity, we show that the proposed parameterization remains qualitatively predictive, reproducing the collision kernel at  $Fr = 0.173$  within acceptable accuracy. A more systematic exploration spanning a broader range of, and lower, Froude numbers is deferred to future work.

Simulations of coalescing droplets have shown that cloud droplet size distributions (DSDs) broaden within short time intervals, even for typical cloud droplets with Stokes numbers around  $St \approx 0.15$ , providing a viable pathway for growth within the bottleneck range. A small fraction of lucky droplets grow disproportionately fast. Whether this arises from mere statistical chance or specifically due to the turbulent flow topology is the subject of future studies. By emulating fluctuations of the local dissipation rate, we found that droplet growth is markedly accelerated in highly dissipative parcels, indicating that intermittency may play an important role in the warm rain process. Depending on droplet size and local turbulence intensity, initially narrow DSDs can broaden as rapidly as wider ones, and at sufficiently elevated dissipation rates, gravitational effects can become practically negligible, underscoring the complex and nontrivial coupling between local flow conditions, the initial droplet population, and its subsequent evolution. Overall, these results support the long-standing hypothesis that turbulent intermittency may contribute to overcoming the bottleneck problem; however, our evidence is limited to Reynolds numbers smaller than those in actual clouds. Numerical simulations are unlikely to reproduce turbulent flows that rival atmospheric conditions in the foreseeable future. Given these constraints, complementary approaches such as high-resolution holographic imaging in clouds appear most promising to clarify this issue.

## ACKNOWLEDGMENTS

This research was supported by funding from the Swiss National Science Foundation (grant 204621). Numerical simulations were carried out using the resources provided by the Euler cluster of ETH Zürich. We thank Arthur Couteau for providing the pseudo-spectral Navier-Stokes DNS solver used in this work.

## AUTHOR CONTRIBUTIONS STATEMENT

L.A.C. performed the simulations. All authors analyzed the results. D.W.M. lead the acquisition of funding. P.J. supervised the project. L.A.C. wrote the original manuscript. All authors reviewed the manuscript.

### Appendix A: Onishi model for the monodisperse radial distribution function

The Onishi model [25] for the monodisperse radial distribution function is

$$g_{ii}(R) - 1 = \begin{cases} A_1 St^2 & (\equiv y_1) \quad (\text{for } St_i < St_a) \\ A_2 Re_\lambda St^{-2} & (\equiv y_2) \quad (\text{for } St_a \leq St_i) \end{cases}, \quad (\text{A1})$$

with  $A_1 = 110$ ,  $A_2 = 0.38$  and  $St_a = ((A_2/A_1)Re_\lambda)^{1/4}$ . The two formulations are connected in the composite expression

$$g_{ii} - 1 = H(St - St_a)y_1 z_a^\alpha + H(St_a - St)y_2(1 - z_a)^\alpha, \quad (\text{A2})$$

where  $H(\cdot)$  denotes the Heaviside function and

$$z_a(St) = \frac{1}{2} \left( 1 - \tanh \frac{\log_{10} St - \log_{10} St_a}{C_a} \right) \quad (\text{A3})$$

with  $C_a = a_c Re_\lambda^{b_c}$ ,  $\alpha = \log_2(a_\alpha Re_\lambda^{b_\alpha})$ ,  $a_c = 0.046$ ,  $b_c = 0.36$ ,  $a_{c2} = 0.094$ ,  $b_{c2} = 0.25$ ,  $a_\alpha = 0.23$  and  $b_\alpha = 0.5$ .

### Appendix B: Wang model for the radial relative velocity

The Wang model [33] for the radial relative velocity is

$$\langle w_r \rangle = \left[ \frac{2}{\pi} (w_{\text{shear}}^2 + w_{\text{accel}}^2) \right]^{1/2}, \quad (\text{B1})$$

with

$$w_{\text{shear}}^2 = \frac{R^2 \varepsilon}{15\nu}, \quad (\text{B2a})$$

$$w_{\text{accel}}^2 = \frac{1}{3} C_w(\phi) f_{KK}, \quad (\text{B2b})$$

$$f_{KK} = \frac{\gamma w_{\text{rms}}^2}{\gamma - 1} \left\{ (\xi_i + \xi_j) - \frac{4\xi_i \xi_j}{(\xi_i + \xi_j)} \left[ \frac{1 + \xi_i + \xi_j}{(1 + \xi_i)(1 + \xi_j)} \right]^{1/2} \right\} \times \left[ \frac{1}{(1 + \xi_i)(1 + \xi_j)} - \frac{1}{(1 + \gamma\xi_i)(1 + \gamma\xi_j)} \right], \quad (\text{B2c})$$

where  $f_{KK}$  was adapted from Kruis & Kusters [45],  $C_w(\phi) = 1 + 0.6 \exp[-(\phi - 1)^{3/2}]$  was provided later on by Zhou et al. [10],  $\phi = \max(St_i/St_j, St_j/St_i)$ ,  $\gamma = 0.183 u_{\text{rms}}^2 / (\varepsilon\nu)^{1/2}$  and  $\xi_i = \tau_{p,i} / (0.4 u_{\text{rms}}^2 / \varepsilon)$ .

### Appendix C: Collision map

The map of collision kernels obtained from the DNS is provided in Table III.

TABLE III. Normalized bidisperse collision kernel  $\Gamma_{ij}/[u_\eta R^2]$  for non-settling droplets mapped across Stokes number pairs. Data obtained from the DNS at  $Re_\lambda = 418$ .

$St_j$	$St_i$												
	0.02	0.04	0.06	0.08	0.10	0.20	0.30	0.40	0.50	0.60	0.70	0.80	
0.02	0.01277												
0.04	0.16505	0.03156											
0.06	0.27601	0.18060	0.04540										
0.08	0.42849	0.32645	0.19559	0.05710									
0.10	0.55848	0.43573	0.38224	0.22440	0.08234								
0.20	1.18572	1.15355	1.08286	1.02224	0.97912	0.37916							
0.30	1.75848	1.76843	1.77923	1.77484	1.76012	1.53078	1.12224						
0.40	2.33210	2.33557	2.37930	2.35424	2.43812	2.49352	2.40884	2.32468					
0.50	2.80317	2.90411	2.94668	2.98532	3.08258	3.31190	3.47191	3.57487	3.83268				
0.60	3.34826	3.37947	3.50426	3.62061	3.67220	4.03588	4.35560	4.67199	4.92353	5.47079			
0.70	3.77795	3.89934	4.03519	4.12801	4.24232	4.68762	5.12753	5.53584	5.94911	6.32796	7.02727		
0.80	4.23107	4.29048	4.47630	4.63539	4.74826	5.28461	5.80139	6.27735	6.76131	7.24059	7.69620	8.47691	
0.90	4.64595	4.79775	4.95827	5.08948	5.23134	5.84230	6.39364	6.94093	7.45838	7.97397	8.47879	8.95773	
1.00	5.04391	5.23472	5.40776	5.49184	5.71050	6.37854	6.94472	7.50873	8.07235	8.60634	9.12294	9.62640	
1.10	5.47413	5.61282	5.78722	5.99485	6.14037	6.84488	7.47552	8.05002	8.60680	9.16491	9.68390	10.19766	
1.20	5.87031	6.07145	6.29976	6.41718	6.56181	7.30054	7.94147	8.55174	9.10734	9.65539	10.17576	10.68197	
1.30	6.26329	6.42922	6.65058	6.80364	6.96769	7.73206	8.38670	8.99183	9.55760	10.10592	10.62200	11.11586	
1.40	6.56997	6.78774	7.01080	7.25122	7.37456	8.13744	8.81393	9.42241	9.98184	10.52753	11.03023	11.53312	
1.50	6.95576	7.13769	7.35240	7.56837	7.73235	8.53061	9.21013	9.80487	10.36470	10.89951	11.41620	11.89506	
1.60	7.24463	7.51275	7.76437	7.93532	8.10387	8.89641	9.58548	10.18556	10.73761	11.27000	11.75116	12.24358	
1.70	7.58767	7.83312	8.11416	8.27969	8.43659	9.25581	9.93697	10.52769	11.08823	11.59651	12.08824	12.56969	
1.80	7.95646	8.15233	8.41134	8.59501	8.77807	9.58937	10.25929	10.85981	11.42777	11.92092	12.41594	12.86127	
1.90	8.27695	8.47734	8.71739	8.89287	9.10369	9.92090	10.59204	11.20353	11.73089	12.23876	12.71681	13.16148	
2.00	8.57909	8.80738	9.04030	9.24321	9.40503	10.23063	10.91301	11.50724	12.04071	12.54522	13.00085	13.45026	

$St_j$	$St_i$												
	0.90	1.00	1.10	1.20	1.30	1.40	1.50	1.60	1.70	1.80	1.90	2.00	
0.90	9.76041												
1.00	10.09796	10.90254											
1.10	10.67080	11.13321	11.89235										
1.20	11.15457	11.60663	12.04728	12.76147									
1.30	11.58628	12.03481	12.46798	12.86599	13.49508								
1.40	12.00200	12.42059	12.84020	13.22151	13.59128	14.16792							
1.50	12.35090	12.77632	13.17037	13.54058	13.88874	14.23512	14.75199						
1.60	12.67264	13.10950	13.50208	13.85476	14.20252	14.50091	14.81292	15.30091					
1.70	12.99965	13.40392	13.78696	14.13359	14.47433	14.77624	15.05530	15.32526	15.75626				
1.80	13.29551	13.69588	14.06014	14.41193	14.73226	15.02399	15.30795	15.55688	15.82958	16.22575			
1.90	13.58672	13.97629	14.32550	14.67578	14.98400	15.27341	15.54030	15.80063	16.03085	16.28500	16.62634		
2.00	13.84152	14.23137	14.58503	14.90659	15.22223	15.50815	15.76992	16.02545	16.24249	16.46829	16.69572	16.99660	

- [1] E. Bodenschatz, S. P. Malinowski, R. A. Shaw, and F. Stratmann, Can We Understand Clouds Without Turbulence?, *Science* **327**, 970 (2010).
- [2] W. W. Grabowski and L.-P. Wang, Growth of Cloud Droplets in a Turbulent Environment, *Annual Review of Fluid Mechanics* **45**, 293 (2013).
- [3] M. R. Maxey, The gravitational settling of aerosol particles in homogeneous turbulence and random flow fields, *Journal of Fluid Mechanics* **174**, 441 (1987).
- [4] K. D. Squires and J. K. Eaton, Preferential concentration of particles by turbulence, *Physics of Fluids A: Fluid Dynamics* **3**, 1169 (1991).
- [5] M. Cencini, J. Bec, L. Biferale, G. Boffetta, A. Celani, A. S. Lanotte, S. Musacchio, and F. Toschi, Dynamics and statistics of heavy particles in turbulent flows, *Journal of Turbulence* **7**, N36 (2006).
- [6] B. Ray and L. R. Collins, Preferential concentration and relative velocity statistics of inertial particles in Navier–Stokes turbulence with and without filtering, *Journal of Fluid Mechanics* **680**, 488 (2011).

- [7] J. Bec, K. Gustavsson, and B. Mehlig, Statistical Models for the Dynamics of Heavy Particles in Turbulence, *Annual Review of Fluid Mechanics* **56**, 189 (2024).
- [8] M. James and S. S. Ray, Enhanced droplet collision rates and impact velocities in turbulent flows: The effect of polydispersity and transient phases, *Scientific Reports* **7**, 12231 (2017).
- [9] V. Nair, B. Devenish, and M. van Reeuwijk, Effect of Gravity on Particle Clustering and Collisions in Decaying Turbulence, *Flow, Turbulence and Combustion* **110**, 889 (2023).
- [10] Y. Zhou, A. S. Wexler, and L.-P. Wang, Modelling turbulent collision of bidisperse inertial particles, *Journal of Fluid Mechanics* **433**, 77 (2001).
- [11] G. Falkovich, A. Fouxon, and M. G. Stepanov, Acceleration of rain initiation by cloud turbulence, *Nature* **419**, 151 (2002).
- [12] M. Wilkinson and B. Mehlig, Caustics in turbulent aerosols, *Europhysics Letters (EPL)* **71**, 186 (2005).
- [13] J. Meibohm, L. Sundberg, B. Mehlig, and K. Gustavsson, Caustic formation in a non-Gaussian model for turbulent aerosols, *Physical Review Fluids* **9**, 024302 (2024).
- [14] L. A. Codispoti, D. W. Meyer, and P. Jenny, Dissecting inertial clustering and sling dynamics in high-Reynolds number particle-laden turbulence, *Physics of Fluids* **37**, 015161 (2025).
- [15] G. P. Bewley, E.-W. Saw, and E. Bodenschatz, Observation of the sling effect, *New Journal of Physics* **15**, 083051 (2013).
- [16] P. Deepu, S. Ravichandran, and R. Govindarajan, Caustics-induced coalescence of small droplets near a vortex, *Physical Review Fluids* **2**, 024305 (2017).
- [17] I. Fouxon, S. Lee, and C. Lee, Intermittency and collisions of fast sedimenting droplets in turbulence, *Physical Review Fluids* **7**, 124303 (2022).
- [18] S. Ravichandran and R. Govindarajan, Waltz of tiny droplets and the flow they live in, *Physical Review Fluids* **7**, 110512 (2022).
- [19] H. Siebert, R. A. Shaw, J. Ditas, T. Schmeissner, S. P. Malinowski, E. Bodenschatz, and H. Xu, High-resolution measurement of cloud microphysics and turbulence at a mountaintop station, *Atmospheric Measurement Techniques* **8**, 3219 (2015).
- [20] B. Thiede, M. L. Larsen, F. Nordsiek, O. Schlenczek, E. Bodenschatz, and G. Bagheri, *Highly Localised Droplet Clustering in Shallow Cumulus Clouds* (2025), [arXiv:2502.19272 \[physics\]](https://arxiv.org/abs/2502.19272).
- [21] N. Allwayin, M. L. Larsen, S. Glienke, and R. A. Shaw, Locally narrow droplet size distributions are ubiquitous in stratocumulus clouds, *Science* **384**, 528 (2024).
- [22] A. B. Kostinski and R. A. Shaw, Fluctuations and Luck in Droplet Growth by Coalescence [10.1175/BAMS-86-2-235](https://doi.org/10.1175/BAMS-86-2-235) (2005).
- [23] R. Onishi and J. C. Vassilicos, Collision statistics of inertial particles in two-dimensional homogeneous isotropic turbulence with an inverse cascade, *Journal of Fluid Mechanics* **745**, 279 (2014).
- [24] R. Onishi, K. Matsuda, and K. Takahashi, Lagrangian Tracking Simulation of Droplet Growth in Turbulence—Turbulence Enhancement of Autoconversion Rate\* [10.1175/JAS-D-14-0292.1](https://doi.org/10.1175/JAS-D-14-0292.1) (2015).
- [25] R. Onishi and A. Seifert, Reynolds-number dependence of turbulence enhancement on collision growth, *Atmospheric Chemistry and Physics* **16**, 12441 (2016).
- [26] P. J. Ireland, A. D. Bragg, and L. R. Collins, The effect of Reynolds number on inertial particle dynamics in isotropic turbulence. Part 1. Simulations without gravitational effects, *Journal of Fluid Mechanics* **796**, 617 (2016).
- [27] S. Sundaram and L. R. Collins, Collision statistics in an isotropic particle-laden turbulent suspension. Part 1. Direct numerical simulations, *Journal of Fluid Mechanics* **335**, 75 (1997).
- [28] L.-P. Wang, A. S. Wexler, and Y. Zhou, Statistical mechanical descriptions of turbulent coagulation, *Physics of Fluids* **10**, 2647 (1998).
- [29] K. Gustavsson and B. Mehlig, Statistical models for spatial patterns of heavy particles in turbulence, *Advances in Physics* **65**, 1 (2016).
- [30] F. Hoffmann, Y. Noh, and S. Raasch, The Route to Raindrop Formation in a Shallow Cumulus Cloud Simulated by a Lagrangian Cloud Model, *Journal of the Atmospheric Sciences* **74**, 2125 (2017).
- [31] K. K. Chandrakar, H. Morrison, W. W. Grabowski, and R. P. Lawson, Are turbulence effects on droplet collision-coalescence a key to understanding observed rain formation in clouds?, *Proceedings of the National Academy of Sciences* **121**, e2319664121 (2024).
- [32] O. Ayala, B. Rosa, and L.-P. Wang, Effects of turbulence on the geometric collision rate of sedimenting droplets. Part 2. Theory and parameterization, *New Journal of Physics* **10**, 075016 (2008).
- [33] L.-P. Wang, A. S. Wexler, and Y. Zhou, Statistical mechanical description and modelling of turbulent collision of inertial particles, *Journal of Fluid Mechanics* **415**, 117 (2000).
- [34] Y. Li, E. Perlman, M. Wan, Y. Yang, C. Meneveau, R. Burns, S. Chen, A. Szalay, and G. Eyink, A public turbulence database cluster and applications to study Lagrangian evolution of velocity increments in turbulence, *Journal of Turbulence* **9**, N31 (2008).
- [35] P. Jenny, M. Torrilhon, and S. Heinz, A solution algorithm for the fluid dynamic equations based on a stochastic model for molecular motion, *Journal of Computational Physics* **229**, 1077 (2010).
- [36] Message Passing Interface Forum, *MPI: A Message-Passing Interface Standard Version 4.0* (2021).
- [37] M. Voßkuhle, A. Pumir, E. Lévêque, and M. Wilkinson, Prevalence of the sling effect for enhancing collision rates in turbulent suspensions, *Journal of Fluid Mechanics* **749**, 841 (2014).
- [38] M. Wilkinson, B. Mehlig, and V. Bezuglyy, Caustic Activation of Rain Showers, *Physical Review Letters* **97**, 048501 (2006).
- [39] L. Pan and P. Padoan, Relative velocity of inertial particles in turbulent flows, *Journal of Fluid Mechanics* **661**, 73 (2010).
- [40] J. Abrahamson, Collision rates of small particles in a vigorously turbulent fluid, *Chemical Engineering Science* **30**, 1371 (1975).

- [41] Y. Zhou, A. S. Wexler, and L.-P. Wang, On the collision rate of small particles in isotropic turbulence. II. Finite inertia case, *Physics of Fluids* **10**, 1206 (1998).
- [42] P. A. Vaillancourt and M. K. Yau, Review of Particle-Turbulence Interactions and Consequences for Cloud Physics, *Bulletin of the American Meteorological Society* **81**, 285 (2000).
- [43] P. J. Ireland, A. D. Bragg, and L. R. Collins, The effect of Reynolds number on inertial particle dynamics in isotropic turbulence. Part 2. Simulations with gravitational effects, *Journal of Fluid Mechanics* **796**, 659 (2016).
- [44] J. Bec, S. S. Ray, E. W. Saw, and H. Homann, Abrupt growth of large aggregates by correlated coalescences in turbulent flow, *Physical Review E* **93**, 031102 (2016).
- [45] F. E. Kruis and K. A. Kusters, The Collision Rate of Particles in Turbulent Flow, *Chemical Engineering Communications* **158**, 201 (1997).